

## Field Monitoring of Negative Skin Friction on Rigid Inclusion Columns under Embankments

Liang Chern Chow, P.E., M.ASCE<sup>1</sup>; Jie Han, Ph.D., P.E., F.ASCE<sup>2</sup>;  
and Gregory R. Reuter, P.E., P.G., D.GE, M.ASCE<sup>3</sup>

<sup>1</sup>American Engineering Testing, Inc., MN. E-mail: lchow@amengtest.com

<sup>2</sup>Univ. of Kansas, CEAE Dept., Lawrence, KS. E-mail: jiehan@ku.edu

<sup>3</sup>American Engineering Testing, Inc., MN. E-mail: greuter@amengtest.com

### ABSTRACT

This paper presents the soil-structure interaction, particularly negative skin friction, of the rigid inclusion columns over a 3.5-year monitoring period. In order to understand the fundamental behavior of rigid inclusions, typical deep foundation and drilled displacement pile approaches were adopted in the analyses. First, the load test results were interpreted to determine the axial capacities and moduli of the rigid inclusion columns. Then, the estimated moduli were used in conjunction with embedded strain gage data in obtaining the axial load distribution profile along the columns from the end-of-construction to post-construction periods, spanning over several years. The strain profile shows that negative skin friction and the neutral plane location progressively developed over time at every instrumented column. Based on that, the neutral plane locations appear to be at 1/2 of the column length, where a stiff clay layer is located. By matching the interpreted loads with the effective stress approach, it was found that the measured  $\beta (= K \tan \delta)$  could range from 0.6 to as high as 2.8, assuming 80% and 20% of load transfer on upper and lower soil layers, respectively. Theoretical  $\beta$  values were also checked against the measured  $\beta$ . It was found that the ratio of  $K/K_0$  arriving at these values was approximately 2.0.

### INTRODUCTION

In 2015, as part of a Minnesota Department of Transportation (MnDOT) pilot project, rigid inclusions were used as a geotechnical solution for a clayey stratum beneath the new interstate highway alignment at the I-35E Cayuga Interchange in St. Paul, Minnesota. The rigid inclusion technique employed in this project was drilled displacement piles or Menard's Controlled Modulus Columns™ (hereinafter, referred to as "columns"). Because geotechnical interests with the use of rigid inclusions consist of evaluating the load transfer mechanism, geotechnical and structural capacities, as well as overall system settlement, an extensive geotechnical instrumentation program was implemented to monitor measurements for these topics. Notably, numerous types of sensors were placed to monitor the deformation and stress response of both individual and groups of the columns. This paper discusses the results from four instrumented columns, one of which was a sacrificial column loaded to failure, and the other three were instrumented with strain gages and load cells.

The rigid inclusion columns were installed by a system described as "augered, pressure-grouted displacement pile" (NeSmith 2002), around which the soil (or material) is displaced horizontally and/or upwardly as the displacement tool advances into the ground. Considering the change in soil stress state during or after construction of the piles, these type of piles are therefore referred to as "displacement" piles. Nonetheless, a critic may question: to what extent of "displacement" or "disturbance" has been altered relative to the initial stress state (of soil)?

When rigid inclusions are used to support embankments, it is well recognized that one of their featured mechanisms is soil arching, under which more overburden stress from the embankment is redistributed to the underlying columns that are relatively stiffer than the surrounding soils, but distributed less to the soils. With new fill placed above these arrays of columns, negative (downward) skin friction arises within the upper portion of the columns when the surrounding soil settles more relative to the columns. Such negative skin friction increases compressive stress in the column and reduces its available axial capacity.

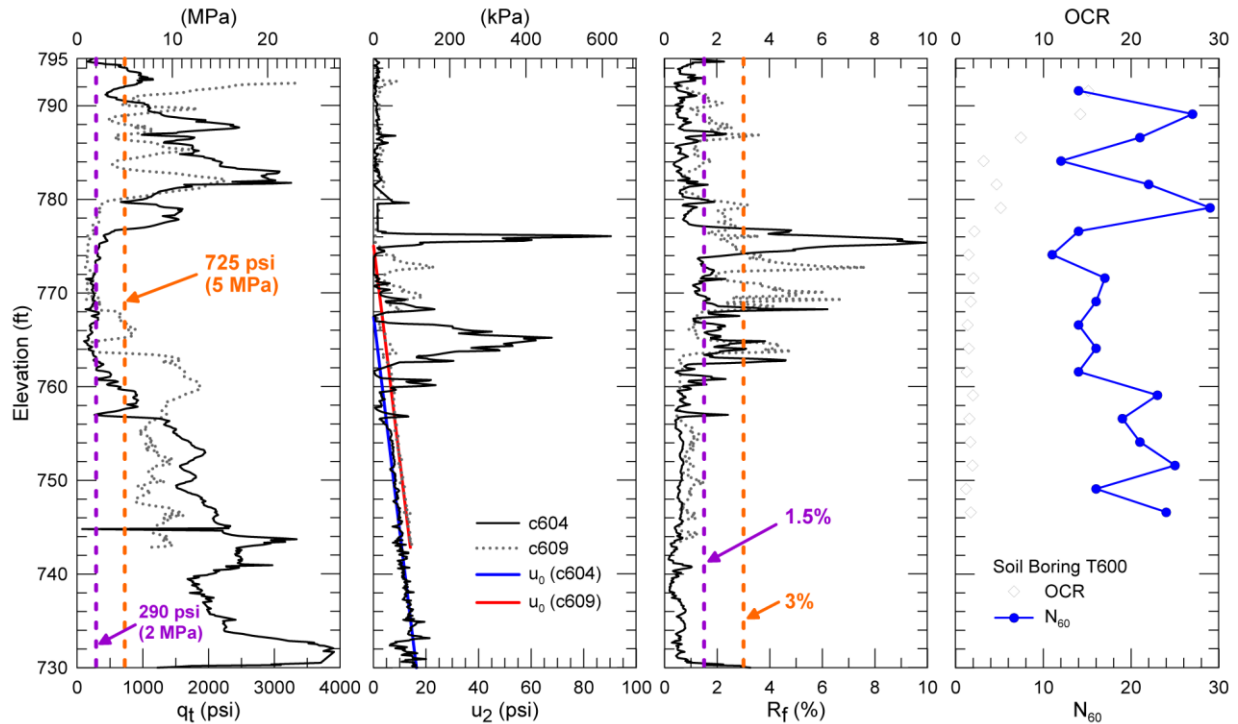


**Figure 1. Nearby piezocone and soil boring results: c604 near test column; c609 and T600 near instrumented columns**

Long-term analysis for negative skin friction can be made with the effective stress approach (Burland 1973). The shear stress ( $\tau$ ) along a column is expressed as the frictional resistance of a shear surface, given by Eqn. (1). For convenience,  $\beta$  can be collectively described as  $K \tan \delta$ :

$$\tau = \beta \sigma'_v = (K \tan \delta) \sigma'_v \tag{1}$$

$$K = K_o (K / K_o) \tag{2}$$

$$K_o = (1 - \sin \phi') OCR^{\sin \phi'} \tag{3}$$

where  $\sigma'_v$  = vertical effective stress,  $\delta$  = effective or drained friction angle ( $\phi'$ ) for the soil-column interface,  $K$  = coefficient of lateral earth pressure ( $\sigma'_h/\sigma'_v$ ),  $K_o$  = in situ coefficient of lateral earth pressure at rest ( $\sigma'_{ho}/\sigma'_{vo}$ ), and OCR = Overconsolidation ratio ( $\sigma'_p/\sigma'_{vo}$ ). Interface friction angle ( $\delta$ ) is normally related to  $\phi'$ . For instance,  $\tan \delta \approx \tan \phi'$  for cast-in-place concrete against soil (i.e. rough interface), such as drilled shaft constructed with a dry method.  $K/K_o$  is, of course, the function of stress state after construction. Depending on the foundation type, construction method, and soil disturbance, the ratio of  $K/K_o$  can vary from 0.5-3.0 (O'Neil 2001, Chen & Kulhawy 2002, Kulhawy & Chen 2007). On the other hand, the parameter  $\beta$  from the effective stress approach depends on the interface friction between soil and pile as well as stress

history. For drilled shafts installed in gravelly soils,  $\beta$  as high as 9 has been reported in Kulhawy & Chen (2007), but on average, falls within the range of 0.24-0.30 in normally consolidated soil. High values of  $\beta$  are generally found within shallow depths of soil profile, but decrease with depth due to decreasing OCR with increasing depth in most natural soil deposits.

## SUBSOIL CONDITIONS

The site was located between Cayuga Street and Maryland Avenue, approximately 3 miles (4.8 km) north of downtown St. Paul, Minnesota. Quaternary geology in this area is described as postglacial (artificial fill over organic or inorganic silt and clay) and middle terrace alluvial deposits, underlain by St. Peter Sandstone, in which the upper part of the formation, the Tonti Member, is about 100 feet (33 m) below grade. Figure 1 presents the results of two CPTu soundings and a nearby soil boring: sounding c604 near the test column; and sounding c609 and soil boring T600 close to the instrumented columns. Based on these sounding profiles, the subsurface condition generally consisted of 10-20 feet (3-6 m) of dense to very dense sand, overlying a stiff clay layer of about 12-15 feet (3.6-4.5 m) thick, followed by medium dense to dense sand. The depth of groundwater was around 17 feet (5.2 m) at sounding c609, but was observed to be deeper, at 28 feet (8.5 m), at c604.

Other nearby soil borings indicate that both the upper and lower sand layers predominantly consisted of fine sand (SP or SP-SM) with or without gravel. Fines content ( $P_{200}$ ) of the soil sampled at the upper sand layer was about 40%, while that at lower sand layer varied between 3% and 49%. The clay layer (elev. 778 to 764) shown in the CPTu soundings, yet, was more variable when compared to the same layer in nearby soil borings in the area. For instance, slightly organic silty clay, highly organic soil, peat, and marl, ranging from very soft to stiff consistencies, were instead classified. Nonetheless, the tip resistance of 290 psi (2.0 MPa) or less, as well as friction ratio ( $R_f$ ) correlation, suggest a Soil Behavior Type of 2 to 3 (organic soils or clay-silty clay) for that layer. Unfortunately, neither in situ testing nor any laboratory testing was conducted on the clay layer. Therefore, compressibility and stress history of the clay layer are unknown.

In Table 1, the subsoil profiles above are divided into several sublayers based on soil type and interpreted soil parameters. The use of tip resistance in estimating preconsolidation pressure ( $\sigma'_p$ ) may not be appropriate for sand and gravelly soil. Therefore, an empirical correlation  $\sigma'_p/P_{atm} = 0.15 N_{60}$  (Kulhawy & Chen, 2007) was used in conjunction with T600 soil boring information.

**Table 1. Subsoil layers and interpreted soil parameters**

Sublayer No.	Soil Type	Elevation (c604)	Avg $\phi'$	Avg OCR <sup>a</sup>
1	Sand (Very dense)	795 – 782	46°	15
2	Sand (Dense)	782 – 775	41°	6
3	Clay (Stiff)	775 – 762	27°	3.5
4	Sand (Medium dense)	762 – 756	32°	1
5	Sand (Dense)	756 – 730	38°	1

<sup>a</sup> Sand layer's OCR was estimated using  $\sigma'_p/P_{atm} = 0.15 N_{60}$  and associated  $\sigma'_{v0}$ ; Clay layer's  $\sigma'_p$  and OCR were correlated with piezocone tip resistance.

## FIELD INSTRUMENTATION & MEASUREMENTS

### Column Load Test Results

During construction, compressive load tests were conducted on two of the rigid inclusion columns per ASTM D1143/D1143M-07 using the Quick Load Test procedure. Each test column was cast with three embedded strain gages along its length to allow for estimation of axial load distribution resulting from the applied top load. This paper only presents the load test result closest to the instrumentation area. The test column was nominally 15.5 inches (394 mm) in diameter and 58.4 feet (17.8 m) in length, with the toe bearing in the sand stratum at elev. 734.5 feet. At this depth, the dense sand was estimated to have  $\phi' = 38^\circ$  based on the normalized cone tip resistance (Robertson & Campanella 1983). Figure 2(a) presents the results from the load test. The test column design load was 114 kips (507 kN), but the specification required the column be tested to 150% (171 kips or 760 kN) or higher of the design capacity. As can be seen, at a top-down load application of 342 kips (1521 kN), the column head reached 0.29 inches (7.4 mm) movement before accumulating greater movement, at which the applied load was perceived, at the time of testing, to be the “failure” load.

Determining the load developed within the columns required an assessment of the axial stiffness ( $EA$ ) of the columns. The best-fit regression line of the stress-strain relationship in Figure 2(a) indicates an elastic modulus of 4,703 ksi (32.4 GPa). Based on this line, it appears that the column did not fail yet, but shaft resistance was fully mobilized after about 0.23 inches of movement. Recognizing that the modulus of concrete is not a constant, but degrades with increasing strain, the tangent modulus method (Fellenius 1989, 2001) was also used. Presented in Figure 2(b), the strain measurements during each loading cycle at three levels (i.e. 2 ft, 21 ft and 57 ft below top of the column) of strain gages are plotted against the tangent modulus. The column top (i.e. G2) strain was not mobilized sufficiently to create a straight line until the third loading cycle, not to mention that the middle and bottom of the column only accumulated very little strains, resulting in extremely high tangent modulus. For better presentation, the tangent modulus diagram is cut off at 1.0 tsf per microstrain to illustrate the modulus degradation trend: based on the regression line, the initial tangent modulus is found to be 0.304 tsf per microstrain or 4,729 ksi (32.6 GPa) that is quite close to the elastic modulus in Figure 2(a).

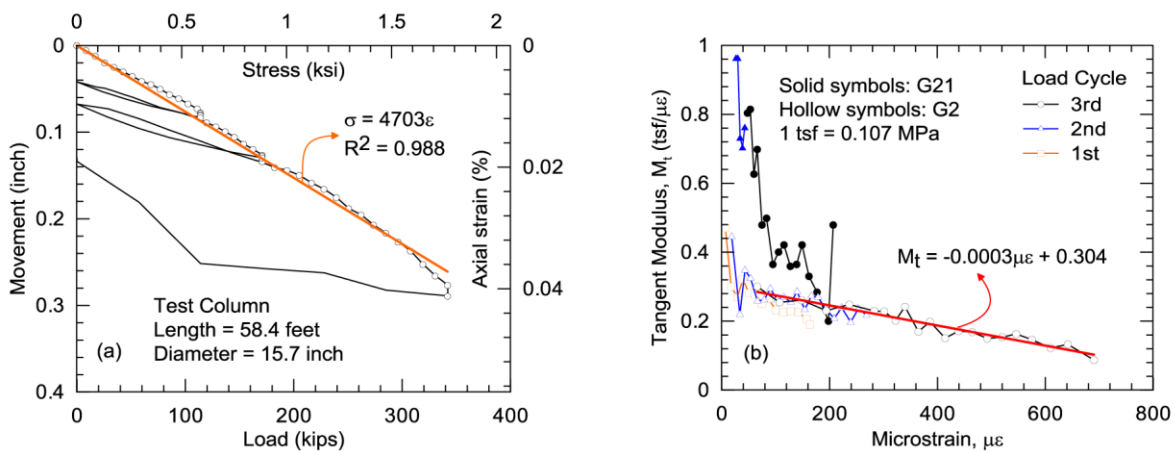


**Figure 2. Test column in the top-down test: (a) load-movement result, and (b) tangent modulus diagram**

## Instrumented Columns

In addition to the load test program, five test areas or “nests” were designated for geotechnical instrumentation and monitoring that included vibrating wire piezometers, load cells, earth pressure cells, sister bar strain gages, and horizontal and vertical ShapeArrays (SAA). In this paper, however, the results from only one “nest” (Nest D) are reported. This nest of instrumentation consists of three columns, each instrumented with a vibrating wire load cell atop and four strain gages placed at various depths along the column: one near the top of the column, two at the top and bottom of the compressible layer, and one within 2 feet of the column toe. The load cell was placed on top of the column, between two 1-inch (25.4 mm) thick customized steel plates, then slightly pre-loaded (i.e. 500 lbs) to a linear range of measurements. Shown in Figure 3 are a schematic view of the cross section and details of load cell installation. In the schematic view, each column is spaced at a 9-foot (2.7 m) square pattern, and followed by the numbers #572, #597, and #622 from left to right. There are two more columns installed beyond #622 (to the right; east), but #572 is the leftmost (westernmost) column at this station. These columns had the same diameter as the test column, but were drilled to a shallower depth of 35.5 feet (10.8 m) or elev. 757.5 feet, bearing on the medium dense sand stratum.

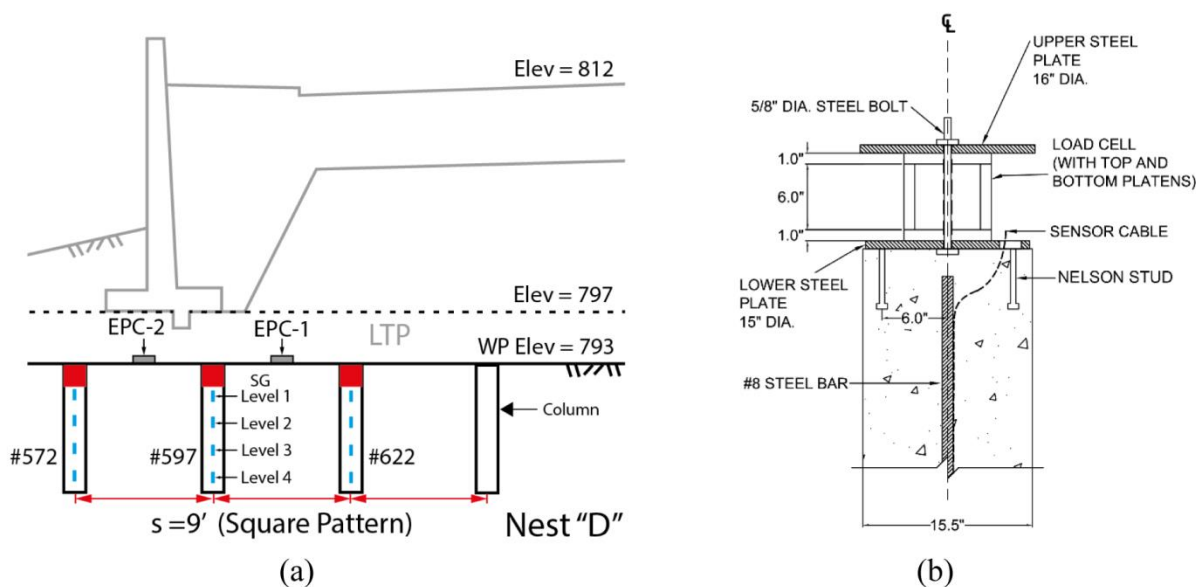


**Figure 3. Schematic view of cross section and load cell configuration**

Figure 4 presents field measurement results from June 2016 until the end of 2018. In the top figure, the load cell measurements refer to change in load relative to initial fill placement, indicating the maximum loads were about 30 kips (133 kN) at columns #597 and #622, while only about one-third of the load was measured at #572 during the entire monitoring period. With a fill height of about 19 feet (5.8 m), the overburden pressure was expected to be 2.3 ksf (109 kPa). Yet, the computed pressures on the columns based on the maximum loads are triple to decuple (10 $\times$ ) of that, i.e. 7.4 and 22.3 ksf (354 and 1,068 kPa), respectively, indicating the evidence of soil arching. Also shown in the figure is the soil pressure measured in between the columns. The soil pressure raised proportionally until about 100 days, after which it became cyclical. By taking an average, the soil pressures are about 2 and 1.2 ksf (96 and 57 kPa) for EPC-1 and EPC-2, respectively. These roughly equate to 88% and 52% of the final overburden

pressure (this is also referred to as the *Stress Reduction Ratio* =  $\sigma_{soil}/\gamma H = \sigma_{EPC}/\gamma H$ ). The order of load transfer is reasonable for stiff soils. The reason behind cyclic measurements is unknown. In the authors' opinion, this could be seasonal temperature fluctuations as the recorded temperatures (from thermistors within the vibrating wire sensors) were used for the thermal correction when correlating for pressure. For this reason, peaks and troughs are repeatedly visible every 300 to 400 days.

The strain measurements from the middle column are also included as an example to illustrate the compressive (negative) strain in response to construction activities. Clearly, all levels of strain accumulated rapidly when the load was sharply increased to about day 180, especially between days 60 and 90. After that, the response remained fairly constant. Nonetheless, the strain continued to gradually increase until about day 480, then approached the final values. This phenomenon demonstrates the soil-structure interaction is time-and-stress dependent especially the transition between days 180 and 480.

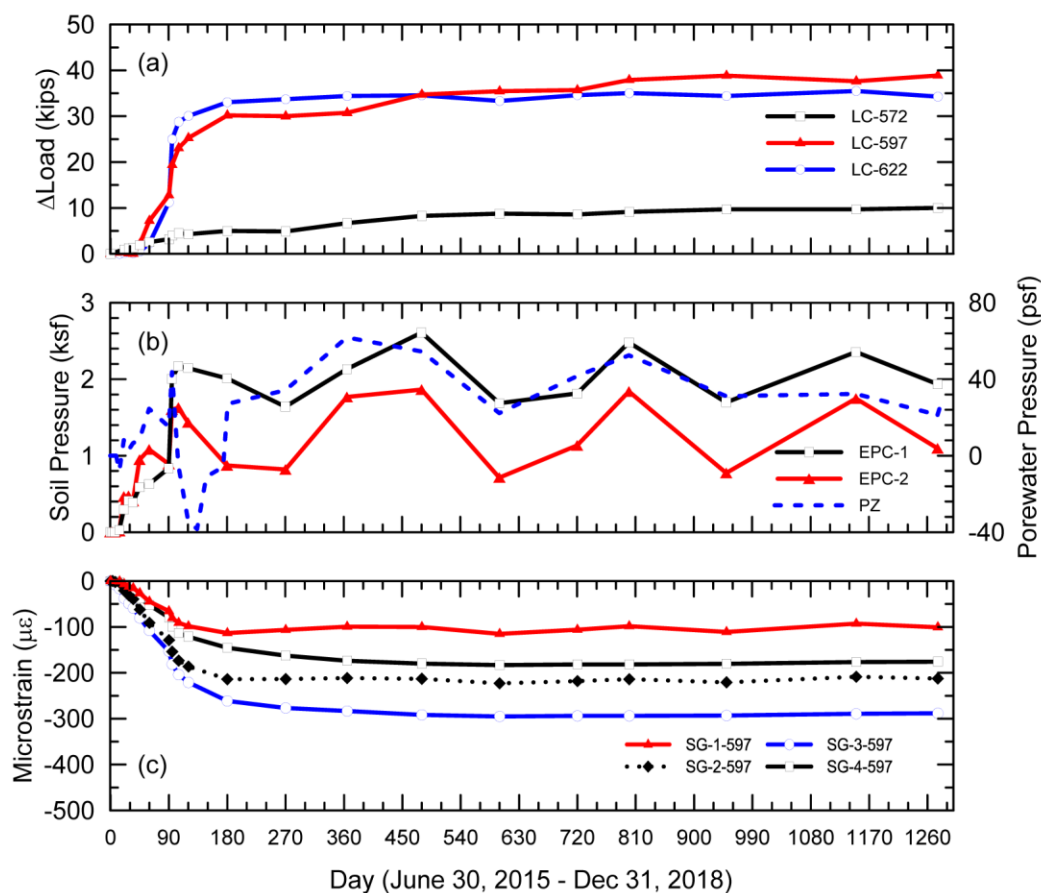


**Figure 4. Monitoring results: (a) load cell (LC) measurements at each instrumented column; (b) soil earth pressure cell (EPC) and piezometer (PZ) measurements in between each column; and, (c) example strain gage (SG) measurements within rigid inclusion #597. 1, 2, 3 and 4 represent strain gage levels.**

## NEGATIVE SKIN FRICTION & ESTIMATION OF $B$

As mentioned earlier, soil arching primarily drives the load transfer onto these columns: (i) soil arching by skin friction, (ii) by arching to the tops of individual columns, and (iii) to the

surrounding soil itself. In other words, even a low level of stress is transferred onto the soil, the following consolidation process leads to the development of negative skin friction along the upper part of the columns. Based on the test column result, it is distinctive that the rigid inclusion column mobilized both skin friction and (partial) toe bearing resistance. Therefore, when both positive and negative skin friction mobilizes, the neutral plane location should be readily identified by the embedded strain gage measurement or profile.

In Figure 5, strain measurements are converted to loads by using the column modulus determined earlier, thereby, creating a depth profile of skin friction at the soil-column interface. Each of the symbols represents a strain gage level, except that the top being the load cell measurements. The load distribution curves indicate that the point at which the maximum axial load (or strain) generally varied with time but tended to remain at the same depth. This maximum load location is known as “neutral plane”, where shear forces reach equilibrium. At this location, no relative settlement occurs between the column and the soil. In this case, the neutral plane is located at the mid-depth (elev. 775±) of the stiff clay as indicated in sounding profile c609. This is contrary to some negative skin friction studies for piles driven into a thick layer of clay, where the neutral plane tends to move downward over time (e.g. Indraratna et al. 1992). The actual shape of load distribution curves just below the maximum point is unknown unless additional strain gage would be installed below. But, based on the subsoil profile, it is improbable that stiff clay and medium dense sand layers would continue to settle. After about day 180, the rate of development of skin friction sharply decreased, converging to the final D-shape curve. The maximum final load was around 320 kips (1,423 kN) at #622. Therefore, the maximum axial compressive stress was 1,650 psi (11.4 MPa). That value would be 66% of the minimum design grout 28-day strength of 2,500 psi (17.2 MPa) but is about 48% of the 3,440 psi (23.7 MPa) average grout strength from the load test columns. The drag load after subtracting measured top load was about 285 kips (1,268 kN).

The compressive stress was developed through negative skin friction, which if not accounted for, can be detrimental to the column structural integrity. By using the effective stress method and neutral plane analysis, the maximum compressive load and drag load can be estimated if column side resistance and dead load are known. However, because of load transfer efficacy, the effective stress method to estimate side resistance is not straightforward but requires some more study.

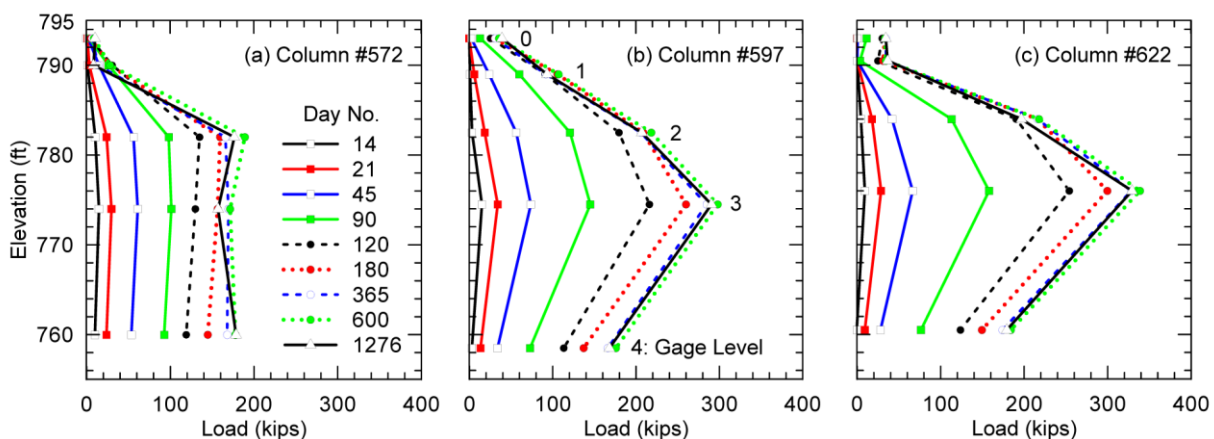


**Figure 5. Measured load distribution along individual instrumented columns. Gage levels represent each strain gage depth, with “0” being load cell at top of the column.**

Shown in Figure 6 are mobilized shear stresses ( $\tau_{mob}$ ) determined by using each level of load distribution curves from Figure 5, then plotted against the corresponding measured load. For example, the “red-circle” line represents the mobilization of shear stress along the segmental surface area between the first and second gages (i.e. a distance of 8 feet) when load was applied on top. In other words, these curves are similar to load-transfer or t-z curves with the replacement of deformation “z”. As can be seen, the  $\tau_{mob}$  values were mostly negative above Gage 3, while below that depth  $\tau_{mob}$  became positive. These  $\tau_{mob}$  values also reveal that skin friction was already or nearly fully mobilized at gage levels 0-1 of column #572, 1-2 of all three columns, 2-3 of #597, and 3-4 of #597 and #622. It is interesting to find that most of the shear stresses were not fully mobilized until after day 180, which is consistent with the observed response earlier. This can be explained by the dissipation of excess negative porewater pressure within the stiff clay layer, which gradually reduced effective stresses over time. For the same reason, the authors think that without any reliable in situ porewater pressure measurement, this modified t-z curve method would work well for assessing  $\beta$ .

By substituting the mobilized shear stress values from Figure 6 into Eqn. (1),  $\beta$  associated with the effective overburden pressure at mid-depth can thus be estimated. For instance, the measured  $\beta$  or  $\beta_m = \tau_{mob} / \sigma'_{vf} = 6.6 \text{ ksf} / (0.69 + 1.71 \text{ ksf}) = 2.8$  at gage level 1-2 of Column #622. Note that the final vertical effective stress ( $\sigma'_{vf} = \sigma'_{vo} + \Delta\sigma'_v$ ) is used because load transfer onto the soil is considered. The determination of final vertical effective stress is discussed next.

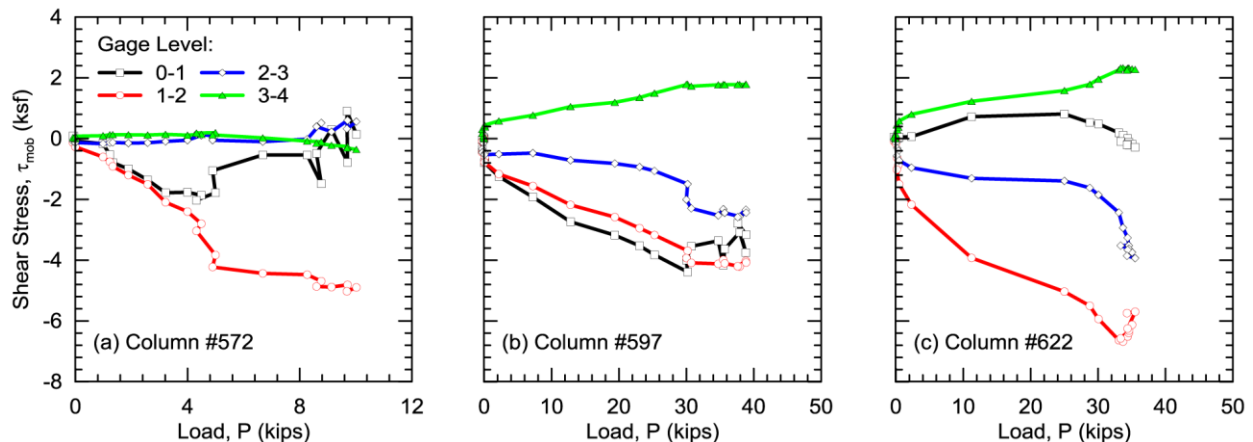


Figure 6. Mobilized shear stress along segments of column over time.

### Vertical Stress Distribution

Unlike conventional effective stress approach for deep foundations, the estimation of  $\beta$  parameters for each sublayer in column-supported embankment raises a question as to what final vertical effective stress ( $\sigma'_{vf} = \sigma'_{vo} + \Delta\sigma'_v$ ) should be used. This stress increment is inherently the load transfer efficacy of CSE or Stress Reduction Ratio ( $SRR = \Delta\sigma'_v / \gamma H$ ). The discussion of load transfer is beyond the scope of this paper, but readers may refer to Russell and Pierpoint (1997), Sloan (2011), and FHWA (2016) for more information. In the reality, the vertical stress distribution may follow that of Westergaard or Boussinesq's solution. Therefore, the final vertical effective stress must be determined before arriving at any  $\beta$  parameters, especially in deeper layer where stress increment is less certain.

By using effective stress approach, the final measured load distribution of columns can be found by matching to the measured load distribution above the neutral plane. Accordingly, the

side resistance ( $R_s = \beta \sigma'_{vf}$ ) can also be determined by using the same  $\beta$  values. Shown in Figure 7(a) is an example of how  $\beta$  values can be found by matching side resistance ( $R_s$ ) to the measured load distribution curve at Column #597. In this figure,  $\Delta\sigma'_v/\gamma H = 0.9$  was assumed, and subsoil profile was divided into five sublayers. The dashed line represents the side resistance ( $R_s$ ) computed based on the blue curve, which matches measured load distribution by varying  $\beta$  values for each sublayer. After some iterative process, a series of  $\beta$  values for each sublayer are formulated. Figure 7(b) combines these  $\beta$  values based on different  $\Delta\sigma'_v/\gamma H$  and superimposes  $\beta_m$  values onto each specific sublayer. For simplification, the vertical stress increments within the top two sublayers was roughly 80% while remaining sublayers was close to 20%. As a result, adjustment of  $\beta_m$  values are needed until achieving convergence. The OCR is also adjusted accordingly. Computed  $\beta_m$  values vary from 0.6 to 2.8, with lower values distributed within the lower sublayers. The unordinary high  $\beta$  of 2.8 is taken from gage level 1-2 of #622. These values are slightly higher than typical  $\beta$  values, but fall within the reasonable range. In term of sensitivity, it is evident that vertical stress increment and  $\beta$  values are less sensitive in deeper soils.

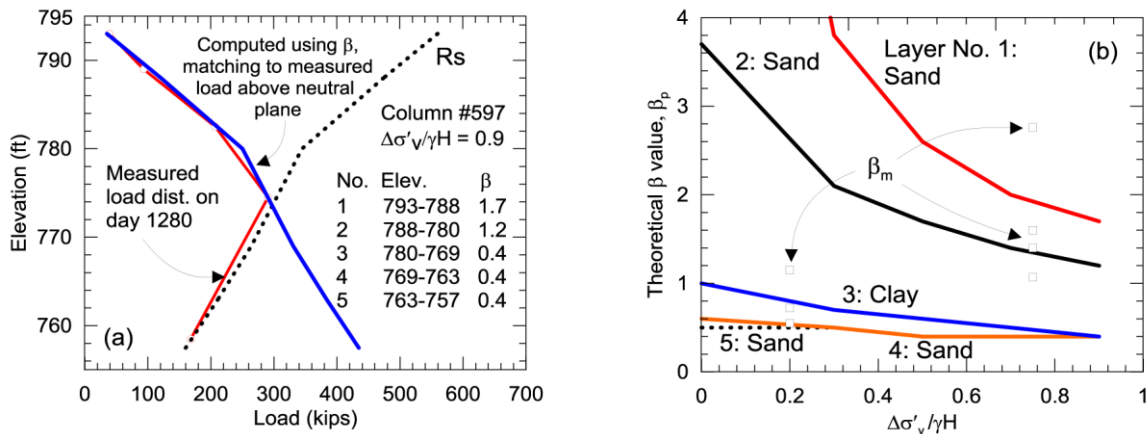


Figure 7. Estimation of vertical stress increment under embankment.

Table 2. Comparison of theoretical and measured  $\beta$  parameters considering stress increment

Soil Type	Elevation (c609)	Avg $\phi'$	Avg OCR <sup>a</sup>	$K/K_o$	$\beta_p$	$\beta_m$
Sand (Very dense)	793 – 790	51.9°	2.4	2.0	1.1	1.1, 1.4 <sup>b</sup>
Sand (Very dense)	790 – 782	43.5°	2.4	2.9	1.6	1.6, 2.8
Clay (Stiff)	782 – 775	27.8°	2.7	2.6	1.1	1.1
Sand (Dense)	774 – 758.5	31.2	1.5	1.8	0.6	0.6, 0.7

<sup>a</sup> OCR =  $\sigma'_p/\sigma'_{vf} = \sigma'_p/(\sigma'_{vo} + \Delta\sigma'_v)$ ; where  $\Delta\sigma'_v = (0.8 \text{ or } 0.2) \times \gamma H$

<sup>b</sup>  $\beta_m = 1.4$  taken from load test result.

Theoretical  $\beta$  or  $\beta_p$  based on the soil parameters interpreted from c609 and Eqns. (2) and (3) are summarized in Table 2. These  $\beta_p$  values were computed by using  $\tan \delta = \tan \phi'$  and changing the ratio of  $K/K_o$ . In general, OCR decreases due to higher vertical stress. One interesting finding is  $K/K_o$  ratios are slightly higher than the range reported for full-displacement driven piles (i.e.

$K/K_0 = 1$  to 2). The high ratio indicates that soil stress is altered and increased after construction for this “augered, pressure grouted” type of drilling system.

## CONCLUDING REMARKS

This paper presents both short-term and long-term monitoring results from the I-35E Cayuga column-supported embankment with rigid inclusions. These monitoring results (axial load distribution) revealed that negative skin friction developed along the upper portion of the column while resisting skin friction developed along the lower portion, forming a D-shape load distribution curve. The vertex of the D-shape curve or maximum compressive stress was close to 70% of the design grout strength. Based on that, the neutral plane locations appear to be at 1/2 of the column length, where a stiff clay layer is located. If effective stress method is coupled with neutral plane analysis, the maximum load can be evaluated for individual column structural integrity or column group capacity. However, because of load transfer efficacy and soil arching, the effective stress approach must consider stress increment to the soil when estimating  $\beta$  values. Further analysis indicated that for drilled displacement type rigid inclusion, both measured  $\beta$  values and  $K/K_0$  ratio are higher than typical values. These findings, however, are limited to data collected from this project.

## ACKNOWLEDGEMENTS

The authors are grateful to Minnesota Department of Transportation (MnDOT) and Menard Group USA for supplying the in situ and load testing data used herein. In particular, the authors would like to acknowledge Rich Lamb, Andrew Eller, Alex Potter-Weight, Joseph Bentler, and Neil Ramdhan for their assistances and contributions on this project.

## REFERENCES

- Burland, J.B. (1973). “Shaft friction of piles in clay – a simple fundamental approach.” *Ground Engineering*, 6: 3-42.
- Chen, Y.-J. and Kulhawy, F.H. (2002). “Evaluation of drained axial capacity for drilled shafts.” ASCE, *International Deep Foundation Congress 2002*, GSP: 1200-1214.
- Fellenius, B.H. (1989). “Tangent modulus of piles determined from strain data.” ASCE, *Geotechnical Engineering Division*, 1989 Foundation Congress, 1: 500-510.
- Fellenius, B.H. (2001). “From strain measurements to load in an instrumented pile.” *Geotechnical News Magazine*, 19(1): 35-38.
- Federal Highway Administration. (2016). *Geotechnical Engineering Circular No. 13 Ground Improvement Modification Methods – Reference Manual Volume II*, FHWA-NHI-16-028.
- Indraratna. B., Balasubramaniam, A.S., Phamvan, P., and Wong. Y.K. (1992). “Development of negative skin friction on driven piles in soft Bangkok clay.” *Can. Geotech. J.*, 29: 393-404.
- Kulhawy, F.H. and Chen, J.-R. (2007). “Discussion of ‘drilled shaft side friction in gravelly soils’ by K.M. Rollins, R.J. Clayton, E.C. Mikesell, and B.C. Blaise.” ASCE, *J. Geotech. and Geoenviron. Eng.*, 133: 1325-1328.
- NeSmith, W.M. (2002). “Static capacity analysis of augered, pressure-injected displacement piles.” ASCE, *Deep Foundation 2002: An International Perspective on Theory, Design and Performance*, Geotechnical Special Publication No. 116: 1174-1186.
- O’Neil, W.M. (2001). “Side resistance in piles and drilled shafts.” ASCE, *J. Geotech. and Geoenviron. Eng.*, The Thirty-Fourth Karl Terzaghi Lecture, 127(1): 3-16.

- Robertson, P.K. and Campanella R.G. (1983). "Interpretation of cone penetration tests. Part I: Sand." *Can. Geotech. J.*, 20(4): 718-733.
- Russell, D., and Pierpoint, N. (1997). "An assessment of design method for piled embankments." *Ground Engineering*, 30(11): 39-44.
- Sloan, J.A. (2011). *Column-Supported Embankments: Full-Scale Tests and Design Recommendations*. Ph.D. Thesis, Virginia Polytechnic Institute.